



Segmentation of the optic disk in color eye fundus images using an adaptive morphological approach

Daniel Welfer^a, Jacob Scharcanski^{a,*}, Cleyson M. Kitamura^b, Melissa M. Dal Pizzol^b, Laura W.B. Ludwig^b, Diane Ruschel Marinho^c

^a Instituto de Informatica, Universidade Federal do Rio Grande do Sul, Av. Bento Gonçalves 9500, CEP. 91509-900 Porto Alegre, RS, Brazil

^b Hospital de Clinicas de Porto Alegre, Rua Ramiro Barcelos, 2350, CEP. 90035-903 Porto Alegre, RS, Brazil

^c Faculdade de Medicina, Universidade Federal do Rio Grande do Sul, Rua Ramiro Barcelos, 2400, CEP. 90035-003 Porto Alegre, RS, Brazil

ARTICLE INFO

Article history:

Received 5 January 2009

Accepted 17 November 2009

Keywords:

Optic disk segmentation

Mathematical morphology

Color fundus image

ABSTRACT

The identification of some important retinal anatomical regions is a prerequisite for the computer aided diagnosis of several retinal diseases. In this paper, we propose a new adaptive method for the automatic segmentation of the optic disk in digital color fundus images, using mathematical morphology. The proposed method has been designed to be robust under varying illumination and image acquisition conditions, common in eye fundus imaging. Our experimental results based on two publicly available eye fundus image databases are encouraging, and indicate that our approach potentially can achieve a better performance than other known methods proposed in the literature. Using the DRIVE database (which consists of 40 retinal images), our method achieves a success rate of 100% in the correct location of the optic disk, with 41.47% of mean overlap. In the DIARETDB1 database (which consists of 89 retinal images), the optic disk is correctly located in 97.75% of the images, with a mean overlap of 43.65%.

© 2009 Elsevier Ltd. All rights reserved.

1. Introduction

Several eye fundus image features are commonly evaluated in computer aided-diagnosis of several retinopathologies [1], such as the retinal blood vessels, the optic disk, and the fovea. The retinal vascular segmentation can be useful, for example, to measure the narrowing of retinal vessels, which is characteristic in hypertense patients [2,3]. The segmentation of blood vessels is important for the detection of non-proliferative diabetic retinopathies, such as venous beading [4–6], and neovascularizations [7,8]. Blood vessels bifurcations also can be used as control points in the retinal image registration and comparison process [9,10]. The detection of the optic disk (papilla) can be important to qualify retina lesions, like the exudate lesions that characterize the diabetic macular edema (DME) [7]. Moreover, optic disk parameters, such as its diameter, allow to detect other retina structures, like the fovea region. For example, Li et al. [11] define the fovea region as a circle located a number of optic disk diameters away from the optic disk center, in the temporal side of the optic disk. Also, based on the size and shape of the optic

disk outer boundaries it is possible to diagnose glaucoma [12]. Next, we discuss representative optic disk detection approaches found in the literature. Afterwards, we briefly discuss the main features of our proposed method, and this paper organization.

1.1. Optic disk detection in the literature

Retinopathologies, such as exudates and/or druses, often appear in retina images as clusters of regions with size and pixel intensities comparable to the optic disk [1]. This makes the detection of the optic disk challenging, since common features such as region size and pixel intensities are unreliable for segmenting the optic disk.

We can divide the methods available in the literature into two groups: the methods that detect the optic disk location but do not detect the optic disk boundary (i.e. that do not segment the optic disk), and the methods that detect the optic disk locus and the optic disk boundary (i.e. that segment the optic disk). Next, we briefly describe these two groups of methods available in the literature.

1.1.1. Methods that do not segment the optic disk

Tobin et al. [13] proposed a method based on spatial filtering and Bayesian classifiers to extract local features from the retinal vasculature, obtaining a confidence image map. The point with the highest confidence value in this confidence image map represents

* Corresponding author. Tel.: +55 51 3308 7128; fax: +55 51 3308 7308.

E-mail addresses: daniel.welfer@inf.ufrgs.br (D. Welfer),

jacobs@inf.ufrgs.br (J. Scharcanski), cmk@hotmail.com (C.M. Kitamura),

melissa.olhos@via-rs.net (M.M. Dal Pizzol), laludwig@hotmail.com (L.W. Ludwig),

diane@portoweb.com.br (D.R. Marinho).

the optic disk center. They reported a performance of 90.4% for the correct optic disk detection. However, since their method uses the visual attributes of the vascular tree to detect the optic disk, their method relies on the accurate detection of the vascular tree (mainly near to the optic disk). The computational cost of their method was not presented. Foracchia et al. [14] identified the main retinal vessels using a parametric model and optimization techniques, and then find the optic disk center based on geometric constraints (e.g. finding the point of convergence of all vessels). They reported 98% of success rate for the correct optic disk detection on a dataset with several images. Park et al. [15] proposed to locate the optic disk according to its morphological properties (i.e. circular area with a large local intensity variability). The local gray level variability existing in the optic disk region was used first by Sinthanayothin et al. [16]. In the region of the optic disk there are blood vessels characterized by low intensity pixel values, and disk fiber tissues characterized by higher intensity pixel values. Thus, the optic disk region typically has higher intensity variation than other eye fundus image regions [16]. However, this method fails if retinopathologies (e.g. bright exudates on a dark local background) are present in the image [17,1]. This happens because the retinopathologies may have a higher intensity variation than the optic disk. Moreover, the diabetic signs (i.e. hard exudates) may appear as clusters of regions with size, contour and pixel intensities comparable to the optic disk [1]. Therefore, the method proposed by Park et al. [15] tends to perform better in images without diabetic signs. They reported a success rate of 90.25% in the optic disk locus detection, but their method do not detect the disk boundaries. Youssif et al. [18] proposed to detect the optic disk using directional filters matched with the outgoing vessels. They report a success rate of 100% for the optic disk detection, but optic disk boundaries are not detected.

1.1.2. Methods that segment the optic disk

Lowell et al. [19] described a method based on a specialized correlational filter to detect approximately the center of the optic disk. They find the optic disk center in almost all usable images (i.e. 96 images of a local dataset, except one), and reported excellent performance in 83% of cases in terms of optic disk contours identification. However, they describe their method as being simple, but do not discuss the computational cost. Niemeijer et al. [20] used an optimized cost function based on a point distribution model to detect retinal structures. They reported a performance of 98.4% for the correct optic disk localization, and a performance in 94% of cases in terms of correct optic disk boundary detection. Sopharak et al. [21] used morphological methods to detect the optic disk in retinal images. They do not discuss the performance for the correct optic disk detection, neither the detection of optic disk boundary performance or the computational cost. Fleming et al. [22] utilized semi-ellipses to detect the optic disk center. They reported 98.4% of success rate for the correct optic disk detection, but numbers to evaluate the optic disk boundary detection were not provided. Carmona et al. [23] utilize a genetic algorithm to detect the optic disk region and the optic disk contour. Their method was tested on 110 images of the retina, and achieve an excellent performance in 96% of the cases for the optic disk contours identification (i.e. having less than 5 pixels of discrepancy when compared with a reference standard). Walter et al. [17] also use a modified variance image method to detect the papilla region. They use alternating sequential filters and a shade-correction operator to reduce the chance of erroneously detecting regions outside the optic disk. The optic disk segmentation is obtained using an optic disk internal point, and a circle as an external marker, and then applying the

watershed transformation to delimit the disk boundaries. However, the outgoing vessels crossing the optic disk can cause difficulties in the outer contour detection. As a result, Walter et al. [17] report 96.6% of accuracy for the optic disk location, and 93.10% of accuracy for the exact optic disk contours identification using a local dataset. Lupaşcu et al. [24], on the other hand, discusses the optic disk locus and boundary detection, and report 95% of success rate in correct optic disk location, and an accuracy of 70% in the optic disk boundary detection (modeling the optic disk as a circle). They utilize texture descriptors and a regression based method to find the most likely circle fitting the optic disk [24].

Therefore, there are methods available in the literature that detect the optic disk location, but do not detect the optic disk boundary. That is, most methods in the literature are not able to automatically detect the optic disk locus and the optic disk boundary. Moreover, most methods proposed to detect the optic disk boundary are influenced by the confluence of outgoing vessels crossing the optic disk region, which results in an inaccurate detection of the optic disk boundary. In this paper, we present a new automatic method that, besides locating the optic disk, it also detects the optic disk boundary. Moreover, our method has been designed to not be negatively affected by the outgoing vessels confluence in the optic disk. Thus, the disk boundary is detected with higher precision. In addition, the computational cost of our method is competitive, and our method does not require the extraction of spatial or statistical features describing the vessels tree, as required by some methods available in the literature.

1.2. Paper structure and contributions

This paper presents an image adaptive method based on a model of the vascular structure to detect the optic disk region. Our approach relies on the use of mathematical morphology techniques and has two main stages, namely: (1) detection of the optic disk location; (2) detection of the optic disk boundary. The optic disk is located using information about the main vessels arcade. Thus, in Section 2.1.1 we present a method for detecting the vascular tree in the eye fundus image. Afterwards, in Section 2.1.2, we described the three steps of the method used to detect an internal point to the optic disk and several other points in the vicinity of this internal point (based on the vascular tree detected as described in Section 2.1.1). Finally, in Section 2.2 we use all the points previously detected inside the optic disk region to identify the optic disk boundary using the watershed transform from markers. Afterwards, the experimental results are discussed in Section 3, and our conclusions are presented in Section 4.

2. Materials and methods

Our proposed method was tested on two databases of retinal images available on the Internet. One of the databases is DRIVE [25], and the other is DIARETDB1 [8]. DRIVE is a database assembled in The Netherlands, and it includes 40 fundus images of 584×565 pixels, captured using a 45° field-of-view fundus camera. DIARETDB1 is a Finnish database consisting of 89 color fundus images of size 1500×1152 pixels, captured using a 50° field-of-view digital fundus camera. These databases contain retina images with diabetic signs, and have a large quality variability (e.g. illumination problems). In order to save computation time, we resized the DIARETDB1 images to 640×480 pixels.

2.1. Proposed method for optic disk location

As mentioned before, our approach uses the vascular tree as a reference to locate the optic disk in images of the retina. This approach was designed to be robust to artifacts that are common when diabetic signs are present in the image (e.g. bright exudates clusters). Normally, the eye fundus image vessels tend to not be affected by these diabetic signs, and can be detected even when such signs exist in the image. In the following section, we present our method for detecting the vascular tree in an eye fundus image.

2.1.1. Detecting the vascular tree

The central idea is to identify the foreground and background of the green channel image f_g . We assume as foreground the brighter structures (e.g. exudates), and as background all the remaining structures (e.g. vessels and hemorrhage). We estimate the background region using the RMIN operator (i.e. which detects the regional minima pixels) [26], followed by a reconstruction by dilation. By detecting the regional minima in the green channel of the original image f_g , we remove the bright areas that potentially are associated with diabetic lesions. In this way a new image, f_1 , is obtained, from which the bright lesions have been removed, as described by

$$f_1 = \mathcal{R}_{f_g}(RMIN(f_g)), \quad (1)$$

where $RMIN(f_g) = \mathcal{R}_{f_g}^*(f_g + 1) - f_g$, and $\mathcal{R}_{f_g}^*(RMIN(f_g))$ are the grayscale reconstruction by dilation using f_g , and $(RMIN(f_g))$ as mask and marker images, respectively; $\mathcal{R}_{f_g}^*(f_g + 1)$ is the grayscale reconstruction by erosion using f_g and $(f_g + 1)$ as mask and marker images, respectively.

Fig. 1(a) illustrates the green channel, f_g , of a color retina image. Fig. 1(b) shows a grayscale image ($RMIN(f_g)$) used as the marker image in Eq. (1). The resultant image f_1 is shown in Fig. 1(c). Note that f_1 virtually does not contain bright spots (i.e. bright regions

that are associated to retinal lesions) in comparison with the original green channel image f_g .

On the f_1 image, we apply the morphological contrast enhancement method proposed by Wirth et al. [27] as specified by

$$f_2 = f_1 + \gamma_{TH}(f_1) - \phi_{TH}(f_1), \quad (2)$$

where the top-hat by opening γ_{TH} is an image which contains only the intensity peaks (i.e. bright regions) of f_1 , and the top-hat by closing ϕ_{TH} is an image that contains only the intensity valleys (i.e. dark regions) of the image f_1 . Then, adding the original image with the top-hat by opening γ_{TH} and then, from this resultant image, subtracting the top-hat by closing ϕ_{TH} , the enhancement of fine details is obtained. In Eq. (2), we use a non-flat structuring element with the shape of an ellipsoid to achieve our enhancement results [27]. The radius of this structuring element was set to 12 pixels and the reference height to gray level 100.

Now, in order to reduce the influence of noise and micro-aneurysms in the detection process, a Gaussian lowpass filtering is performed on f_2 with a standard deviation $\sigma = 2.5$ and a mask size of $6\sigma \times 6\sigma$ [28,29], as specified by

$$f_3 = f_2 * G(x, y), \quad (3)$$

where

$$G(x, y) = \frac{1}{2\pi\sigma^2} \exp\left(-\frac{x^2 + y^2}{2\sigma^2}\right). \quad (4)$$

Next, we wish to extract low intensity regions (i.e. local minima) that also are elongated. These will be associated with the retinal vascular tree, and will be used later to locate the optic disk. Therefore, we enhance local minima, detect elongated local minima, and obtain a binary mask with the retinal vascular tree. To enhance local minima, we first apply a top-hat by closing [26] on the image f_3 , as shown below

$$f_4 = \phi_{TH}^{(B)}(f_3), \quad (5)$$

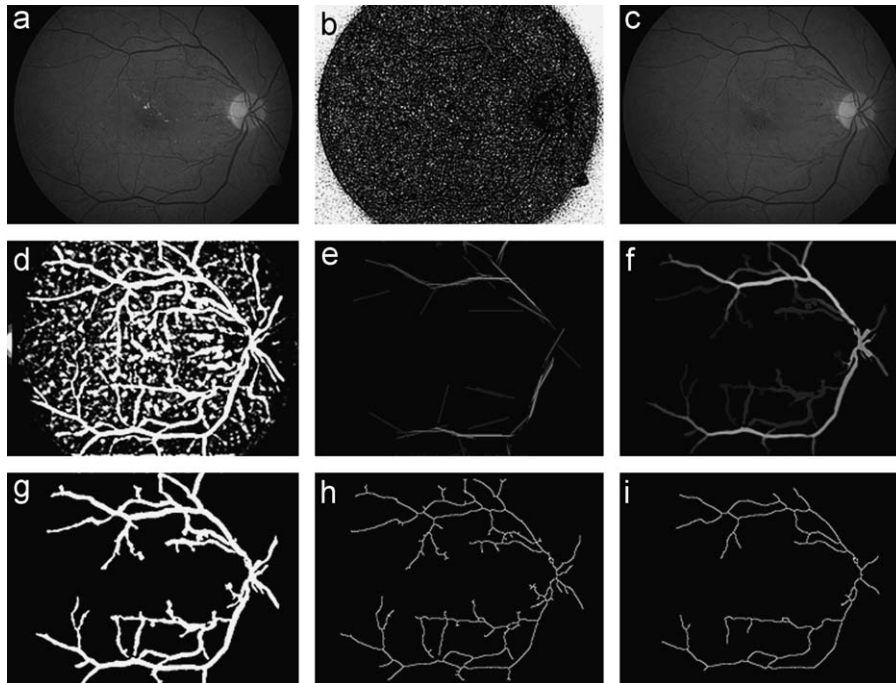


Fig. 1. Steps for vessel segmentation: (a) original image f_g , (b) image marker derived from RMIN operator, (c) f_1 background image derived from Eq. (1), (d) f_4 : top-hat by closing of image f_3 , (e) f_5 : supremum of openings of f_4 , (f) f_6 : reconstruction of image f_5 using image f_4 as mask image, (g) f_7 image: complement of the regional minima of the image f_6 , (h) f_8 skeleton image, (i) f_9 image obtained after 20 pruning cycles on image f_8 .

where B is a flat, diamond-shaped, structuring element larger than the maximal width of vessels. We used in this work a diamond-shaped structuring element with a side of 10 pixels. Applying the top-hat by closing transform, only the local minima (i.e. vessels) of the image f_3 are enhanced (see image f_4 illustrated in Fig. 1(d)).

The next step consists of the calculation of the supremum of openings of f_4 , by a set of linear structuring elements [29,28]. The goal of the supremum of openings is to identify only elongated structures (i.e. vessels) in the image f_4 . We use 24 linear structuring elements, each with 80 pixels of length (i.e. 1×80), designed to fit the main vessels of the arcade in the right and left eyes. The supremum of openings operation is defined by

$$f_5 = \left(\bigcup_{R_\theta=1}^{12} \gamma^{(B_{R_\theta})}(f_4) \right) \cup \left(\bigcup_{L_\theta=1}^{12} \gamma^{(B_{L_\theta})}(f_4) \right), \quad (6)$$

where B_{R_θ} are structuring elements used to detect the superior and inferior main vessels in the right eye using as angles of rotation: $R_\theta = \{15^\circ \dots 90^\circ; -15^\circ \dots -90^\circ\}$; and B_{L_θ} are structuring elements used to detect the superior and inferior main vessels of the left eye, using as angles of rotation $L_\theta = \{105^\circ \dots 180^\circ; 195^\circ \dots 270^\circ\}$.

The image formed by the supremum of openings consists of a set of line segments, as shown in Fig. 1(e). Now, the vascular tree is estimated by the morphological reconstruction by dilation operation [28], using f_4 as a mask image and f_5 as the marker image, according to

$$f_6 = \mathcal{R}_{f_4}(f_5). \quad (7)$$

The resulting image f_6 is illustrated in Fig. 1(f). However, f_6 is a grayscale image and we wish to identify the vessel regions by logical values (i.e. value “1” for vessels and “0” for the background). Thus, applying the above described RMIN operator to get all regional minima of the f_6 image, we obtain a binary image where all non-vessels structures of this image have value “1”. Thus, making an image complement, we mark as “1” the pixels that represent the vessels. Fig. 1(g) shows the resultant image f_7 obtained by Eq. (8), that specifies this vessel extraction process:

$$f_7 = (RMIN(f_6))^c. \quad (8)$$

The morphological skeleton [30] of the binary image f_7 was then obtained as shown below:

$$f_8 = SKEL(f_7), \quad (9)$$

where SKEL represents the skeletonization process of the image f_7 .

Finally, the last step for detecting the vascular tree is an image pruning of f_8 . The pruning algorithm uses the hit-or-miss templates suggested in [30] to detect and to remove all binary image endpoints of f_8 image. For example, to remove 20 pixels at each endpoint, 20 sequential pruning cycles are needed. We call f_9 the image containing the pruned morphological skeleton. Fig. 1(i) shows f_9 image obtained after 20 cycles of the pruning algorithm on the f_8 image (the number of pruning cycles was determined experimentally).

The flowchart in Fig. 2 illustrates the algorithm, step-by-step, used to obtain a binary image, which represents the skeleton of the retinal vascular tree.

2.1.2. Locating the optic disk

Given the detected vascular tree image f_9 (see an illustration in Fig. 1(i)), the algorithm to locate the optic disk is described step-by-step below.

Step 1: In this step, we find the optic disk position, that is, if it is located in the right or in the left image side. An iterative method is proposed for this task and its pseudocode is shown in Algorithm 1.

Algorithm 1. Pseudocode to find the optic disk position.

Input: pruned image (f_9)

Output: optic disk position

- 1 $f_9^{(1)} =$ binary image f_9 with holes filled;
- 2 $f_9^{(2)} =$ skeletonized image of $f_9^{(1)}$;
- 3 **for** $i \leftarrow 3$ **do** n **do**
- 4 $\downarrow f_9^{(i)} =$ pruning of the previous $f_9^{(i-1)}$ image;
- 5 Find the centroid (C_x, C_y) of the above $f_9^{(n)}$ image;
- 6 Find the endpoints of the $f_9^{(n)}$ image using hit-or-miss templates;
- 7 Find the most distant endpoint (E_x, E_y) from centroid point (C_x, C_y);
- 8 **if** $C_x > E_x$ **then**
- 9 \downarrow the arcade is located in the left side and the optic disk is in the right side;
- 10 **else**
- 11 \downarrow the arcade is located in the right side and the optic disk is in the left side;

The purpose of the Algorithm 1 is to reduce the image f_9 to a curve that represents the inferior and superior arcades, as illustrated by Fig. 3(f), find the centroid and the endpoint of this curve most distant from the centroid, and finally in which image side the optic disk is located. In order to obtain the curved shape of the external vessel arcade, firstly we fill all the holes of the image f_9 (line 1, of the Algorithm 1). Fig. 3(a) illustrates that a hole occurs in the skeleton image f_9 as a result of the interweaving of vessels, as indicated by the white arrows. Fig. 3(b) illustrates when all these holes are filled, and their pixels are assigned to “1”. Eq. (10) shows the closing-of-holes operator proposed by Dougherty and Lotufo [30], which is used to fill all the holes in the binary image f_9 .

$$f_9^{(1)} = (\mathcal{R}_{g_{hole}}(f_{hole}))^c, \quad (10)$$

where f_{hole} is a marker image of same size as f_9 , but whose foreground pixels are located only in the image margins (i.e. $f_9(0,0)$). The mask image g_{hole} is the complement of the original image f_9 . Thus, using f_{hole} and g_{hole} , a reconstruction by dilation $\mathcal{R}_{g_{hole}}$ is performed. Then, the complement of this reconstructed image $(\mathcal{R}_{g_{hole}})^c$ results in an image with all holes filled.

Next, the morphological skeleton of the image $f_9^{(1)}$ (image with holes filled according to line 1 of Algorithm 1) is obtained. The morphological skeletonization performed on image $f_9^{(1)}$ results in the removal of the areas represented by the holes of $f_9^{(1)}$. This step is shown in line 2 of Algorithm 1, and the resultant image $f_9^{(2)}$ is illustrated in Fig. 3(c). Next, we perform n (i.e. $n = 100$ in all our experiments) pruning cycles on the skeletonized $f_9^{(2)}$ image (line 4 of Algorithm 1), and obtain the image $f_9^{(n)}$ illustrated by Fig. 3(f). Thus, now it is possible to obtain the external vessel arcade centroid point (C_x, C_y) using image $f_9^{(n)}$. The centroid of the $f_9^{(n)}$ image (C_x, C_y) is a reference point close to the optic disk region, and is calculated according to

$$C_x = \sum_{i=1}^{\kappa} \frac{x_i}{\kappa}, \quad C_y = \sum_{i=1}^{\kappa} \frac{y_i}{\kappa}, \quad (11)$$

where x_i and y_i are the coordinates of pixel $f_9^{(n)}(x_i, y_i)$ in the binary image $f_9^{(n)}$, and κ is the number of pixels set to “1” in this binary image, that is, the number of external vessels arcade pixels.

Anatomically, most part of the vessel arcade curve is located in the temporal side of the optic disk. The temporal side is the opposite side of the optic disk, that is, if the optic disk is in the

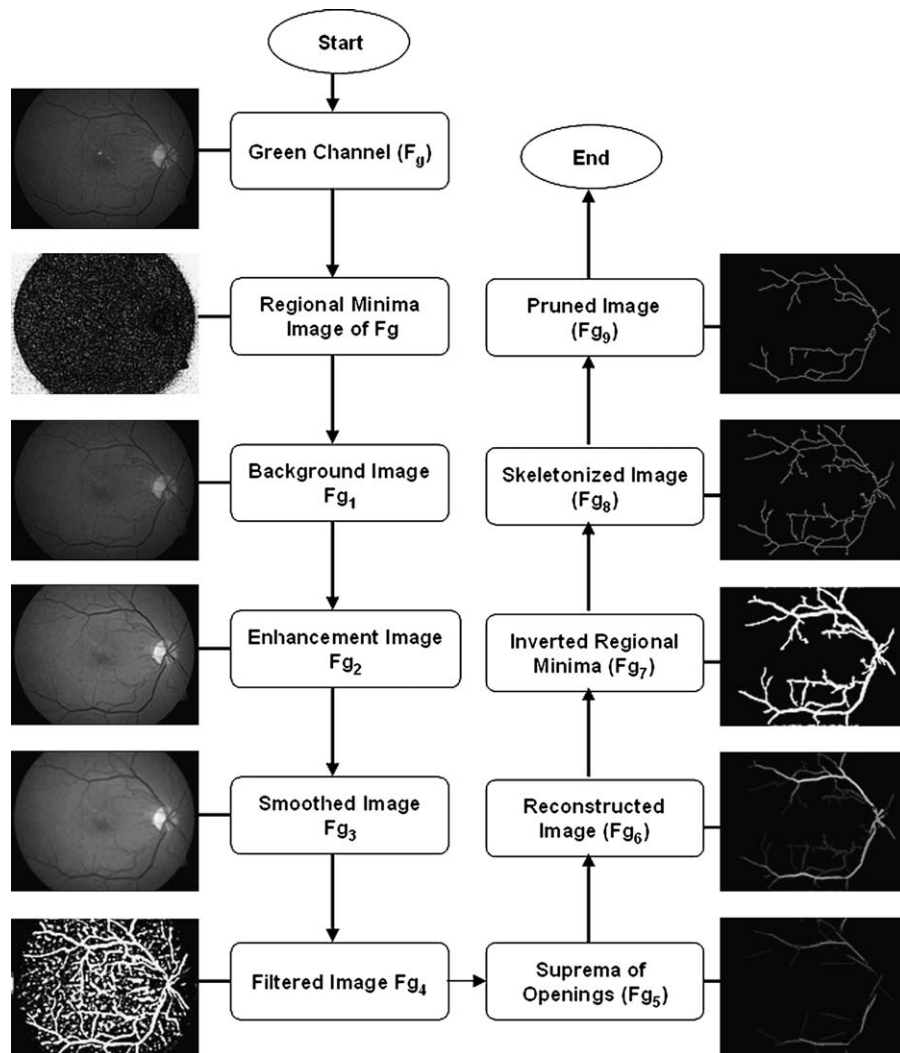


Fig. 2. Summarized steps to detect the vascular tree.

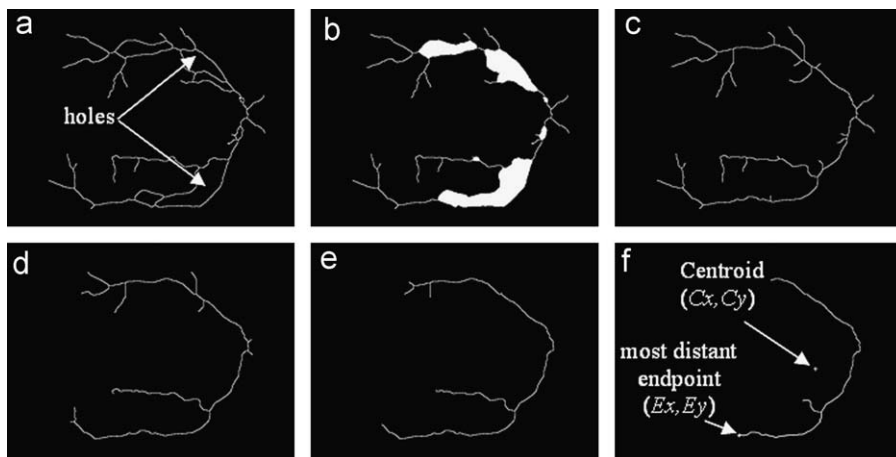


Fig. 3. Detecting the arcade curve: (a) original image f_9 where the white arrows are indicating two holes, (b) $f_9^{(1)}$ image (from Algorithm 1) with all their holes filled, (c) $f_9^{(2)}$ image (from Algorithm 1) which is the skeleton of the image $f_9^{(1)}$, (d) $f_9^{(n)}$ image after 20 pruning cycles, (e) $f_9^{(n)}$ image after 40 pruning cycles, (f) $f_9^{(n)}$ image after 100 pruning cycles indicating the centroid point and the most distant endpoint from the centroid.

right side of the image (i.e. as illustrated in Fig. 3), the temporal side is located in the left side of the image. Then, using the centroid (C_x, C_y) as a reference point for the optic disk location,

and another point, namely (E_x, E_y) , which represents the endpoint of the vessel arcade curve in image $f_9^{(n)}$ most distant to the centroid (see lines 5 and 7 of Algorithm 1), we can find the optic disk

position (i.e. left or right image side). If the column position of the centroid point (C_x, C_y) has a higher value than the column position of the most distant endpoint (E_x, E_y) (see Fig. 3(f)), then the optic disk is in the right side of the image. Otherwise, the optic disk is in the left side of the image. This step is shown in line 8 of the Algorithm 1.

However, it shall be observed that the Algorithm 1 also will work properly on optic disk centered images, whose temporal arcades are outside of the image. In the case of these images, the Algorithm 1 attempts to identify the optic disk position using the superior and inferior nasal arcades (i.e. the arcades that are located in the opposite side of the temporal arcades).

Step 2: Given the optic disk position (i.e. if optic disk in the right or left image side), we locate approximately the optic disk. This can be done removing less important vessels from f_9 (i.e. the pruned image illustrated in Fig. 1(i)). It is important to note that image $f_9^{(n)}$ (see Fig. 3(f)) cannot be used for the approximate optic disk localization, because the procedure that removes the image holes (by filling holes followed by a morphological skeletonization) changes the original location of the main vessels arcade curve and of its center (i.e. the main vessels arcade center). Thus, we exclude all vessels located in the temporal side of the centroid (C_x, C_y) of the image f_9 using a vertical line as a reference (see Fig. 4(a)). The pixel where this vertical line crosses the main vessels arcade in the binary image f_9 also is removed (i.e. receives value “0”), now making part of the background of the image f_9 , and cutting the external arcade curve in different connected sets of pixels. This reference vertical line is drawn passing through the (C_x, C_y) centroid of the image f_9 , and causes a rupture in the main vessels arcade since all pixels belonging to this vertical line are assigned to “0”.

The white arrows in Fig. 4(b) show the exact locations where the main vessels arcade are interrupted. We call f_{10} the image with the vessels interrupted by the vertical line, and in which

there may be several connected binary regions (i.e. vessels arcade fragments). In the next step, the vertical line is translated towards the optic disk image side (since we already know the side of the optic disk, see step 1). In our experiments the horizontal translation was set to 10 pixels, as shown in Fig. 4(c). As illustrated in Fig. 4, the optic disk is at the right side of the image, and at this stage the vertical line is now located at the right side of the pixel where the vessels arcade was interrupted (the opposite would be true if the optic disk was in the left side of the image).

Continuing the explanation of our algorithm based on the example of Fig. 4, next we perform a binary image difference between the image depicted in Fig. 4(c) and the image f_{10} (see Fig. 4(b)), and obtain a binary image where only the vertical line is present. We call this binary image, where only the vertical line is present, the marker image f_{10}^m . Finally, using a reconstruction by dilation with f_{10}^m as a marker image, and using the image f_{10} as the mask image, we obtain only the portion the vessels arcade in the image f_{10} located nearer to the optic disk. Fig. 4(d) shows the image f_{11} obtained from this binary reconstruction by dilation defined by

$$f_{11} = \mathcal{R}_{f_{10}}(f_{10}^m). \quad (12)$$

Step 3: In this step, we describe how the optic disk is located in the image f_{11} . A new centroid (C'_x, C'_y) is calculated for the reconstructed image f_{11} (see Figs. 4(d) and 5(a)). Next, all the holes (the closed areas formed by interweaving of vessels) of the binary image f_{11} are filled using the closing-of-holes operator previously described in Eq. (10). Let f_{12} be the image f_{11} after holes filling, as illustrated by Fig. 5(b). Next, the image f_{12} is skeletonized (see Fig. 5(c)) and then pruned (see Section 2.1.1) to remove small tree branches (see Fig. 5(d)), and obtain the image foreground skeleton. We call this pruned image f_{13} (it is illustrated in Fig. 5(d)), and has been obtained using β pruning cycles (i.e. $\beta = 40$ in all experiments). Next, we follow a horizontal line

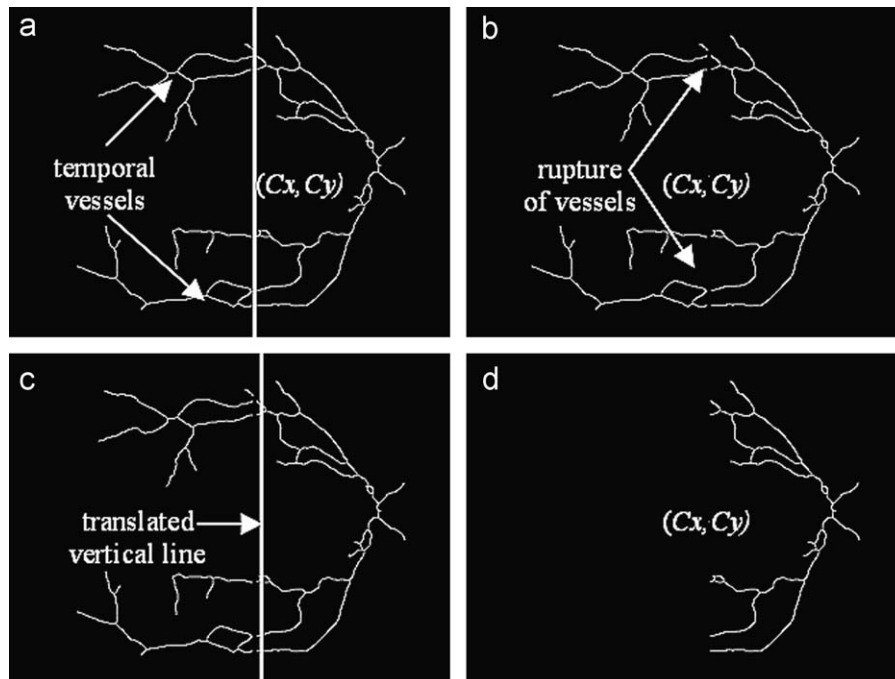


Fig. 4. (a) Pruned f_9 image with a vertical line (f_{10}^m marker image) in the foreground; (b) f_{10} image showing the rupture in the vessels of the skeleton caused by subtraction between f_9 image and the f_{10}^m marker image; (c) the vertical line (foreground of the f_{10}^m image) is moved (translated) some positions in the optic disk direction; (d) image f_{11} obtained from the binary reconstruction by dilation using the translated vertical line as a marker image and the f_{10} as mask image.

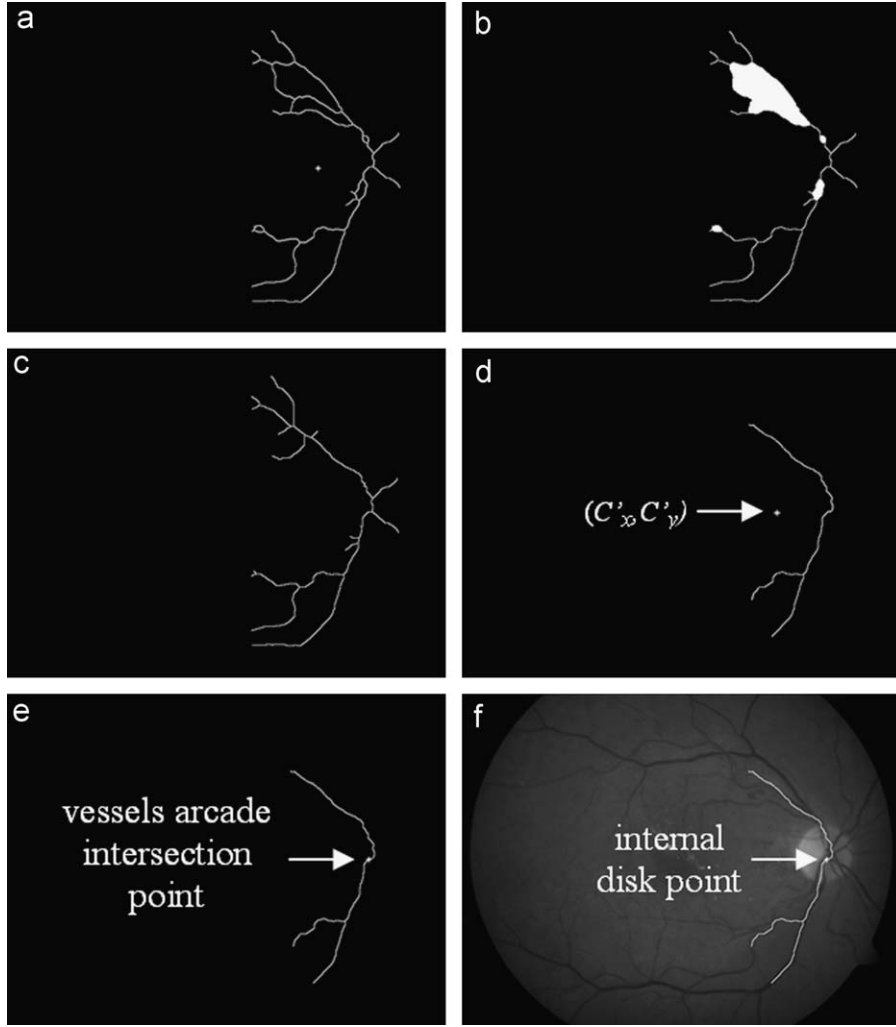


Fig. 5. Main stages to find an internal optic disk point according to our approach: (a) f_{11} image with its centroid indicated by the white arrow, (b) resultant f_{12} image obtained by the closing-of-holes operator performed on the image f_{11} , (c) image obtained after performing a skeletonization on the image f_{12} , (d) f_{13} image obtained pruning the skeletonized version of the image f_{12} , (e) point where the main vessels arcade fragment is intercepted by the horizontal line, (f) the intercepted point likely to be internal to optic disk (I_x, I_y) .

starting at (C'_x, C'_y) and move towards the optic disk searching for an internal point of the optic disk. The intercept of this horizontal line and the main vessels arcade fragment of the image f_{13} provides this optic disk internal point. This point is likely to be inside the optic disk because the horizontal line intercepts the main vessels arcade close to its central part (i.e. inside the optic disk). Fig. 5(e) illustrates this horizontal line intersection point with the fragment of the main vessels arcade in image f_{13} , and Fig. 5(f) shows image f_{13} and the detected internal disk point overlaid on the green channel.

However, it shall be observed that in some cases, the horizontal line will not intercept the central part of the main vessel arcade at a single point. This effect is caused by the pruning algorithm we used, which does not guarantee the elimination of less relevant vessels in the vicinity of the optic disk center. So, in these cases, first we calculate the average position of all intercepted points, and then we use this average position as the internal optic disk point. Nevertheless, since we do not need an internal optic disk point located exactly on the optic disk center, this average position tends to be sufficient for the desired accuracy.

Let the detected internal optic disk point be (I_x, I_y) . Next, (I_x, I_y) will be used to locate the optic disk boundary adaptively in the vicinity of (I_x, I_y) . The optic disk boundary is detected by a region growing method, using as seeds the pixels connected to (I_x, I_y)

on the main vessels arcade fragment in f_{13} , as explained in Section 2.2.

2.2. Proposed method for optic disk boundary detection

In this section, we discuss how to use the point internal to the optic disk (I_x, I_y) , and the main vessels arcade curve fragment of f_{13} in the neighborhood of (I_x, I_y) , to detect the boundaries of the optic disk. Algorithm 2 describes the proposed method step-by-step.

In order to find the optic disk boundary, we use the watershed transform from markers [30], with internal and external markers. As internal markers, we use a list of k pixels of the main vessels arcade of f_{13} in the vicinity of (I_x, I_y) (in our experiments, $k = 20$, above and below (I_x, I_y)). As external markers, we use a circle of constant diameter, centered at each pixel of $\{K_{(I_x, I_y)}^i\}$, where $i = 1, \dots, k$. Then, using the watershed transform from markers with the internal and external markers as parameters, several optic disk boundary shapes are obtained. That is, in our case, we obtained 20 boundary shapes, each one centered at one internal marker $\{K_{(I_x, I_y)}^i\}$. Fig. 6(a)–(d) shows four of these boundary shapes (appearing as white irregular contours). Among the k boundary shapes, we select that one with the highest compactness and

largest area as an estimate of the optic disk boundary shape. The compactness of a shape can be calculated using the formula presented [31] below:

as an estimate of the optic disk boundary and will be used later to identify the refined estimate of the optic disk boundary. Using this estimated boundary shape, we obtain new internal and external

Algorithm 2. Pseudocode to find the optic disk boundaries.

```

input  $K$  pixels of the main
vessels arcade of  $f_{13}$  in the vicinity of  $(I_x, I_y)$  ( $\{K_{(I_x, I_y)}^i\}$ )
output boundaries of
the optic disk
1 foreach  $\{K_{(I_x, I_y)}^i\}$  do
2   On the red image channel (of the original color image), remove large peaks using a morphological opening;
3   Reconstruct the previously morphological opened image;
4   Find the morphological gradient of the previously reconstructed image;
5   Select the  $\{K_{(I_x, I_y)}^i\}$  point as an internal marker
6   Draw a circle of predefined size, centered in the  $\{K_{(I_x, I_y)}^i\}$  point, and use it as an external marker;
7   Perform the Watershed Transformation from Markers on the above gradient image using these markers;
8   Get the optic disk boundary and the shape area returned by the previously described Watershed Transform;
9   Calculate the compactness criterion;

10 Select the optic disk boundary with the highest compactness and largest area;
11 Perform a morphological erosion on this selected optic disk boundary and use it as a new internal marker;
12 Draw a new circle of predefined size, centered in the above eroded optic disk boundary, and use it as a new
external marker;
13 Perform a new Watershed Transformation from markers using the markers found in the previous step;
14 Output the refined estimate of the optic disk boundary obtained using the Watershed Transformation in the
previous step.

```

$$\text{Compactness} = \frac{C^2}{A}, \quad (13)$$

where C is the boundary shape perimeter and A the shape area. The optic disk boundary shape of Fig. 6(d) represents the shape with the highest compactness and largest area. Thus, it is selected

markers. We do a morphological erosion on this selected boundary shape, and use it as a new internal marker. We experimentally chose a diamond structuring element of size 10 to perform this erosion. The white filled shape in Fig. 6(e) depicts an example of this internal marker. As external marker, we use a circle centered in the previous internal marker. The radius of this circle must be

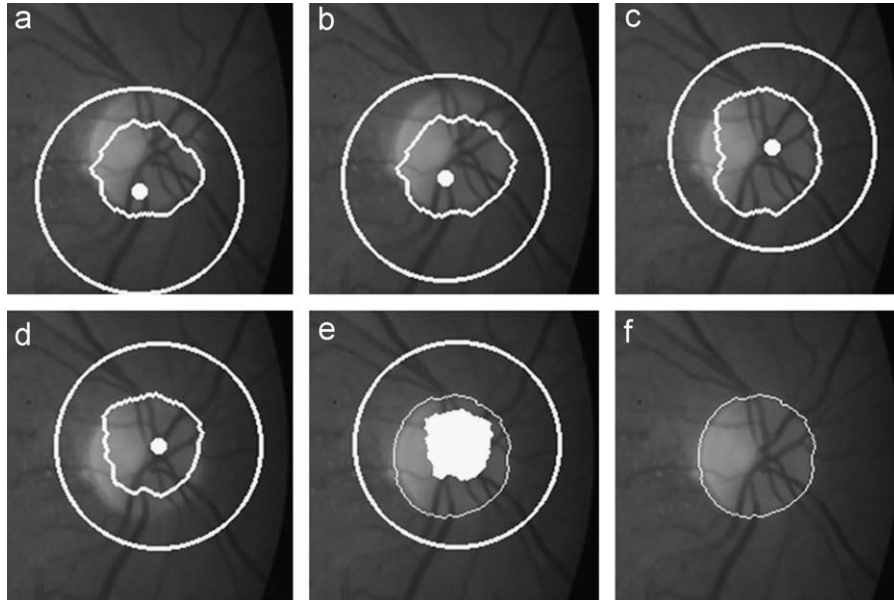


Fig. 6. Detecting the optic disk boundaries. (a)–(d) shows four optic disk boundaries (appearing as white irregular contours) detected using the watershed transformation from markers from each $\{K_{(I_x, I_y)}^i\}$ point. The largest white circle depicts the external marker and the white filled small shape depicts the internal marker. (e) The white filled shape is the boundary shape with the highest compactness and largest area after a morphological erosion. This white filled shape is used as a new internal marker and a circle of predefined size centered in this white filled shape is used as a new external marker. The middle shape represents the refined estimate of the optic disk boundary obtained using the watershed transform with these last markers. (f) Final optic disk boundary obtained in (e) overlaid on the green channel.

larger than the optic disk radius to ensure that the entire optical disk is within the circle. We used a radius equal to 70 pixels in our experiments, and the largest white circle in Fig. 6(e) represents this external marker. Thus, using the watersheds transform from markers with these new two markers (i.e. internal and external), a refined optic disk boundary estimate is obtained. The middle shape in Fig. 6(e) (i.e. the white shape with irregular contour) represents this refined estimate of the optic disk boundary. Fig. 6(f) shows the final boundary overlayed on the green channel.

Algorithm 2 is based on the proposed work of Walter et al. [17], but with four differences. The first difference consists on the number of internal markers we used. Walter et al. use a single point as internal marker, but we use a list of promising points as internal markers (i.e. $\{K_{(i,j)}^i\}$). The use of a single point as an internal marker to find the optic disk boundary may be problematic, since several vessels may be located in the neighborhood of this point. For example, if the internal marker point is located far from optic disk center, and it is located in the neighborhood of large vessels, the watershed transform from markers [30] may detect these vessels as part of the disk boundary. Walter et al. [17] try to minimize this problem by applying several morphological operators, but it requires to know in advance the vessels width to choose a suitable structuring element (since a constant structuring element size may cause the segmentation to fail). The second difference refers to the preliminary optic disk boundary that our proposed method detects. Walter et al. detect only the final optic disk boundary, but our method detects a list of promising boundaries. The third difference refers to the analysis step implemented by our method, since it detects the preliminary boundary shape (i.e. from a list) with the highest compactness and largest area. Finally, the fourth difference consists in the fact that we use the preliminary boundary shape as a new internal marker, which is used to detect the refined estimate of the optic disk boundary.

3. Experimental results

We tested our method on the 40 images of the DRIVE database, and on the 89 images of the DIARETDB1 database. The same parameter values are used in our method for these two image databases, i.e. in the vascular tree detection, in the optic disk localization, and in the optic disk boundary detection.

First, we evaluated the optical disk location performance, and after that we evaluated the disk boundaries identification performance. Using the DRIVE database, our method correctly located the optic disk in 100% of the images, and using the DIARETDB1 the success rate for the localization of the optic disk was 97.75% (i.e. 87 correct optic disk detections in a total of 89 images).

The reason for the failure in only two images was due to an incorrect identification of the vascular tree by the method described in Section 2.1.1. Due to the large amount of opaque lesions (e.g. hemorrhages) just between the end of the main vessels arcades, the semi-ellipses shape of the arcades could not be detected. Thus, for this reason, the method to find the optic disk locus failed.

Table 1 summarizes the results obtained by methods available in the literature and by our proposed method in relation to the optic disk location (using DRIVE and DIARETDB1 databases). The results indicate that our method provides promising results compared to other available techniques. To achieve these results, we considered correct all optic disk locations detected within the borders of the optic disk marked manually. Moreover, it shall be observed that in order to obtain results for both databases, we have implemented and tested all methods presented in Table 1.

Table 1

Success rate in the optic disk location using the proposed method and other methods available in the literature (DRIVE and DIARETDB1 databases).

Methods ^a	Detection performance (DRIVE database) ^b (%)	Detection performance (DIARETDB1 database) ^b (%)
Sopharak et al. [21]—Mathematical Morphology	95	59.55
Walter et al. [17]—Mathematical Morphology	77.5	92.13
Șap̃or et al. [32]—Mathematical Morphology	87.5	78.65
Seo et al. [33]—Labeling and Canny	95	80.89
Lupașcu et al. [24]—Circle that fits the optic disk	95	86.51
Kande et al. [34]—Geometric active contour model	95	88.76
Our proposed method	100	97.7

^a We have implemented all methods, and tested them on the DRIVE and DIARETDB1 databases.

^b We considered correct all automatically detected optic disk location that is within the borders of the optic disk marked manually.

Table 2

Computational cost of our proposed method using the DIARETDB1 dataset.

	Average time per image (s)	Total time (min)
Optic disk location	7.89	11.70
Optic disk boundary detection	4.28	
Total	12.17	18.05

In terms of optic disk location and optic disk boundary detection, our approach tends to have a low computation complexity when compared with other methods reported in the literature. This happens because we do not use the variance calculation nor morphological alternating sequential filters with large structuring elements, as Walter et al. [17].

For all images of the DIARETDB1 database, for example, our method takes 18.05 min (see Table 2) and the approaches proposed by, for example, Walter et al. [17] and Kande et al. [34] take 174.49 (average time of 117.63 s per image) and 108.05 (average time of 72.84 s per image) min, respectively. In this way, our method can be seen as an interesting option to handle large image sets. Our experiments were performed using a PC-based system with Intel(R) Core(TM)2 Quad CPU, clock of 2.40 GHz, and 4 GB of RAM memory. It shall be observed that the above mentioned performance numbers relate to measurements based on our implementations of the method in Table 1.

Next, we evaluate of the optic disk boundary detection in both databases. We use the area overlap and the mean absolute distance (MAD) [11,35] to evaluate the segmentation results obtained by our method. In our work, the optic disk center and contour of each image has been labeled by four ophthalmologists as suggested in [19]. Afterwards, the mean labeled contour was calculated, and then it was used as ground truth. The area overlap between the ground truth optic disk region and the optic disk region obtained by our proposed method was estimated as

$$\text{overlap} = \frac{TP}{TP + FN + FP}, \quad (14)$$

where TP, FN, and FP are the occurrences of true positive, false positive and false positive pixels, respectively. In addition, we also

use the mean absolute distance (MAD) [11,35] to measure the boundary detection accuracy between our method and the approach proposed by literature. Fig. 7 shows an intuition of the true positives, false positives, false negatives, and the true negative areas. The left circle of Fig. 7 represents the optic disk manually segmented, and the right circle illustrates the optical disk that was automatically segmented.

Table 3 shows the results obtained (i.e. in terms of area overlap and MAD) by our method using the DRIVE and the DIARETDB1 database in detail. According to Table 3, our method achieves a mean overlap of 41.47% and 43.65% on the DRIVE and DIARETDB1, respectively. Table 3 summarizes the optic disk boundary identification results achieved by methods proposed in the literature, and by our method, indicating that our method significantly improves on the results achieved by other methods proposed in the literature. It shall be observed that our method potentially can provide the highest overlap, with one of the smallest MAD values. Also, our method can detect the optic disk in all images of the DRIVE database, and detects the optic disk in more images of the DIARETDB1 database than other methods available in the literature.

The method proposed by Walter et al. [17] has a lower correct optic disk boundary detection rate because, as they describe in [17], the influence of outgoing vessels cause optic disk contour irregularities. They tried to improve it by to reducing the vessels influence using a morphological closing with a large hexagonal structuring element, but it was not sufficient as the results show. The structuring element must be bigger than the maximal vessel

width to be effective, and this poses difficulties since the vessels vary in widths in different images; besides, it is challenging to identify the vessels width with precision. This is illustrated in the images of Fig. 8. It shall be observed that if the structuring element used is too large, besides decreasing the performance of the method, it does not guarantee that all traces of the vessels are removed. Moreover, a very large structuring element may deform the boundary of the optic disk.

In our approach, we use a large region as internal marker (e.g. as the solid white area in Fig. 6(e)) for detecting the optic disk boundary with a watershed transform. This large internal marker reduces the vessels influence on the detection of the optic disk boundary, improving the segmentation reliability.

In all images of Fig. 8, it is possible to see that the large blood vessels inside the optic disk did not affect the identification of the optic disk boundaries. However, the images (g)–(l) in Fig. 8 illustrate the major drawback of our approach. In the images (h), (k), (l) the distortion in the boundary identification occurred due to internal marker, which was selected to detect the final optic disk contour (line 11, of Algorithm 2). This selected internal marker, even after a morphological erosion, exceeded the disk boundary limit and caused the distortion in the boundary identification in these images.

For example, in Fig. 8(h), the internal marker exceeds the disk in the south direction. As a result, the boundary located below the part of the disk center was wrongly detected. When an internal marker has a shape that exceeds the disk boundary, part external to the disk is marked as an internal region causing then the contour distortion. In the images (g), (i) and (j) of Fig. 8 the contrary happened, that is, the internal marker automatically selected was very small and did not cover the area where vessels were predominant.

Thus, the bad segmentation results reported by our method were not caused by a wrong location of the internal point. They were caused by the selected contour shape which exceeded the disk boundary limit when it was used as internal marker.

The boundary detection accuracy of our method was evaluated with the mean absolute distance (MAD) too. The MAD [35,11] performs a contour-based analysis of the disk and does not use area regions like the overlap metric uses. The MAD is computed using the optic disk ground truth images as references. A zero MAD value indicates perfect boundary detection, in other words, an exact matching between the boundary of the optic disk labeled manually and the automatic methods. The bigger the MAD value,

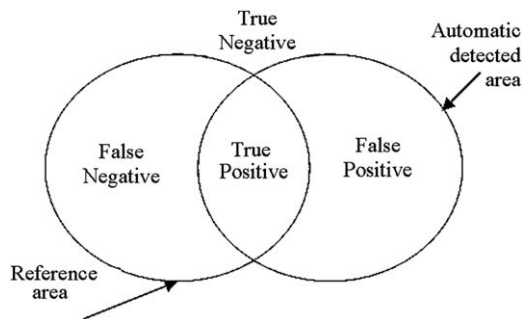


Fig. 7. Areas used to find the overlap measure.

Table 3

Success rate for the identification of the optic disk rim according to the proposed and other methods of the literature using the DRIVE and DIARETDB1 databases.

Methods	DRIVE database			
	Average overlap (%)	± standard deviation overlap (%)	Average MAD	± standard deviation MAD
Sopharak et al. [21]	17.98	6.23	20.94	15.57
Walter et al. [17]	30.03	13.22	12.39	8.27
Seo et al. [33]	31.60	9.71	11.19	4.06
Kande et al. [34]	28.68	7.88	17.42	8.06
Stăpor et al. [32]	32.47	15.17	9.85	6.00
Lupașcu et al. [24]	40.35	8.43	8.05	7.61
Our proposed method	41.47	8.33	5.74	
Methods	DIARETDB1 database			
	Average overlap (%)	± standard deviation overlap (%)	Average MAD	± standard deviation MAD
Sopharak et al. [21]	29.79	9.81	16.31	5.35
Walter et al. [17]	37.25	11.86	15.52	5.32
Seo et al. [33]	35.33	7.65	9.74	4.65
Kande et al. [34]	33.18	5.29	8.35	3.20
Stăpor et al. [32]	34.10	9.98	6.02	5.64
Lupașcu et al. [24]	30.95	13.48	13.81	9.11
Our proposed method	43.65	10.91	8.31	4.05

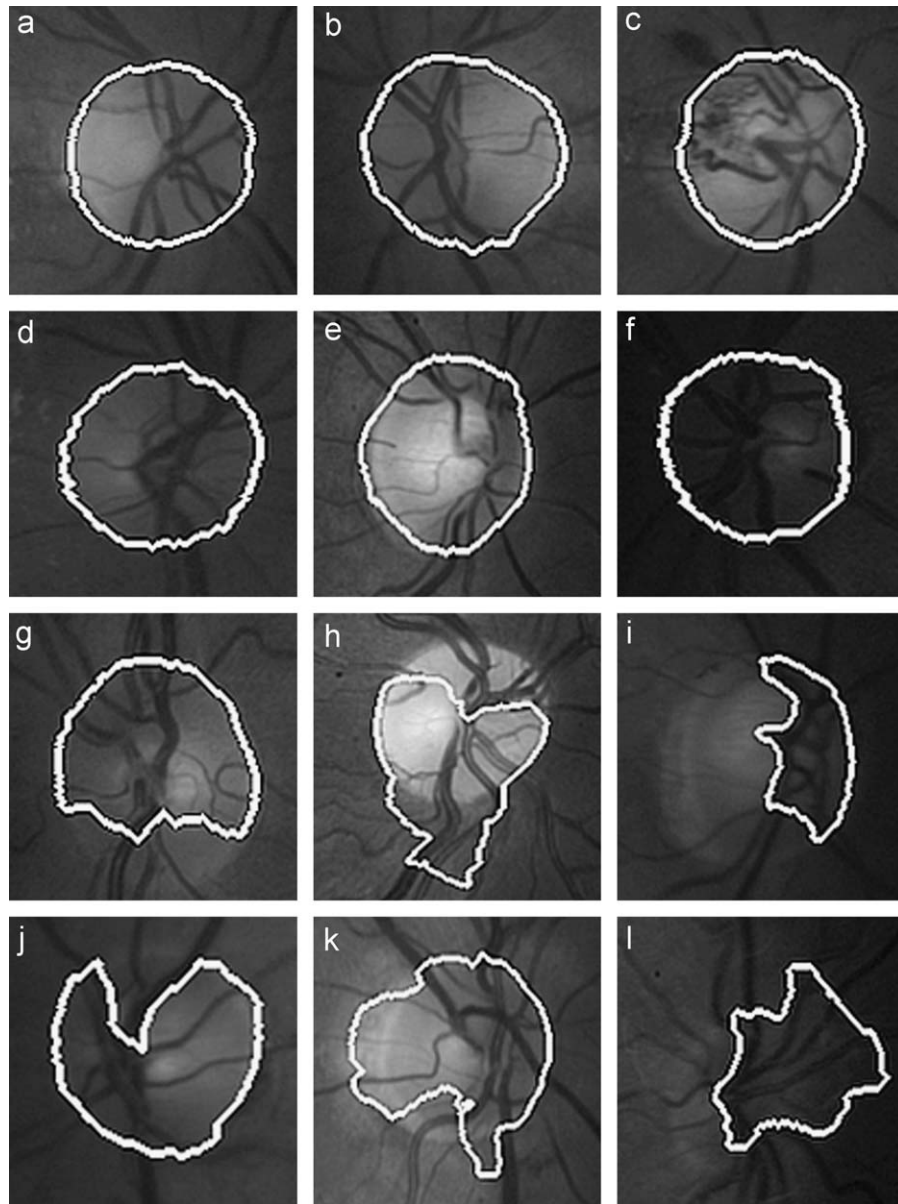


Fig. 8. Classification of the results using our approach. (a)–(f): good; (g)–(l): bad optic disk segmentation.

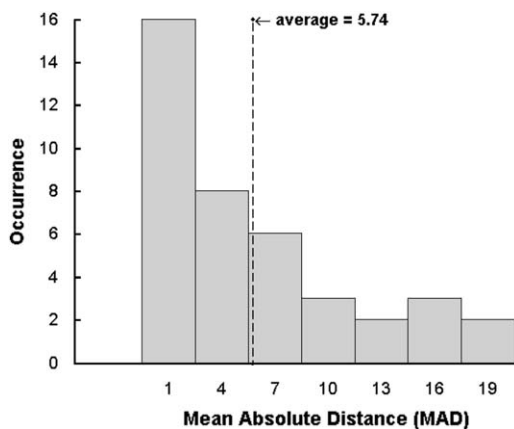


Fig. 9. Proposed method histogram for all images of the DRIVE database according to MAD measure (the measured standard deviation is 5.28).

the worst is the accuracy in the detection of the disk contour. For example, the MAD obtained for the first image of the DRIVE database was of 2.63 pixels using our approach and of 4.48 pixels using the method proposed by Walter et al. [17]. So, for this first image we achieve a better segmentation because we are nearer of the ground truth contour of the optic disk. Table 3 summarizes the average MAD achieved by methods proposed in the literature, and by our method, indicating that our method report the lowest average MAD on the DRIVE database and, consequently the best optic disk boundary identification. On the DIARETDB1 database the method proposed by Stapor et al. [32] achieves the lowest average MAD however, our overlap value was largest.

Since several retinal images of the DRIVE database contain large confluences of vessels located within and crossing the optic disk region, the method proposed by Walter et al. was not able to detect accurately the optic disk contour in most retinal images of this dataset (i.e. resulting in large MAD values). As the method of Walter et al. uses a single point as internal marker to

detect the optic disk, the outgoing vessels of large width cause optic disk contour irregularities. Moreover, as they use a circle of fixed radius centered on the internal point as external marker, the

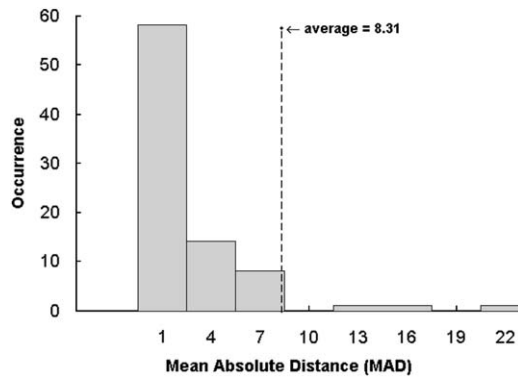


Fig. 10. Proposed method histogram for all DIARETDB1 images using the MAD analysis (the measured standard deviation is 4.05).

external region to the optic disk may be wrongly detected causing then the contour distortion. The method proposed by Kande et al. [34] is also very negatively influenced by blood vessels in the optic disk region, which resulted in a high average MAD. Figs. 9 and 10 show the performance of our approach for all images of the DRIVE and DIARETDB1 databases, respectively. As it can be observed in Figs. 9 and 10, a similar MAD distribution is found for both databases, and small MAD values are more frequent.

Fig. 11 illustrates the robustness of our method in various situations, such as varying illumination and acquisition conditions, and different diabetic lesions.

4. Conclusions and future work

This paper introduces a new adaptive method based on mathematical morphology to identify some important optic disk features namely, the optic disk locus and the optic disk rim.

The proposed method was tested on two publicly available databases, DRIVE and DIARETDB1. For the DRIVE database, we

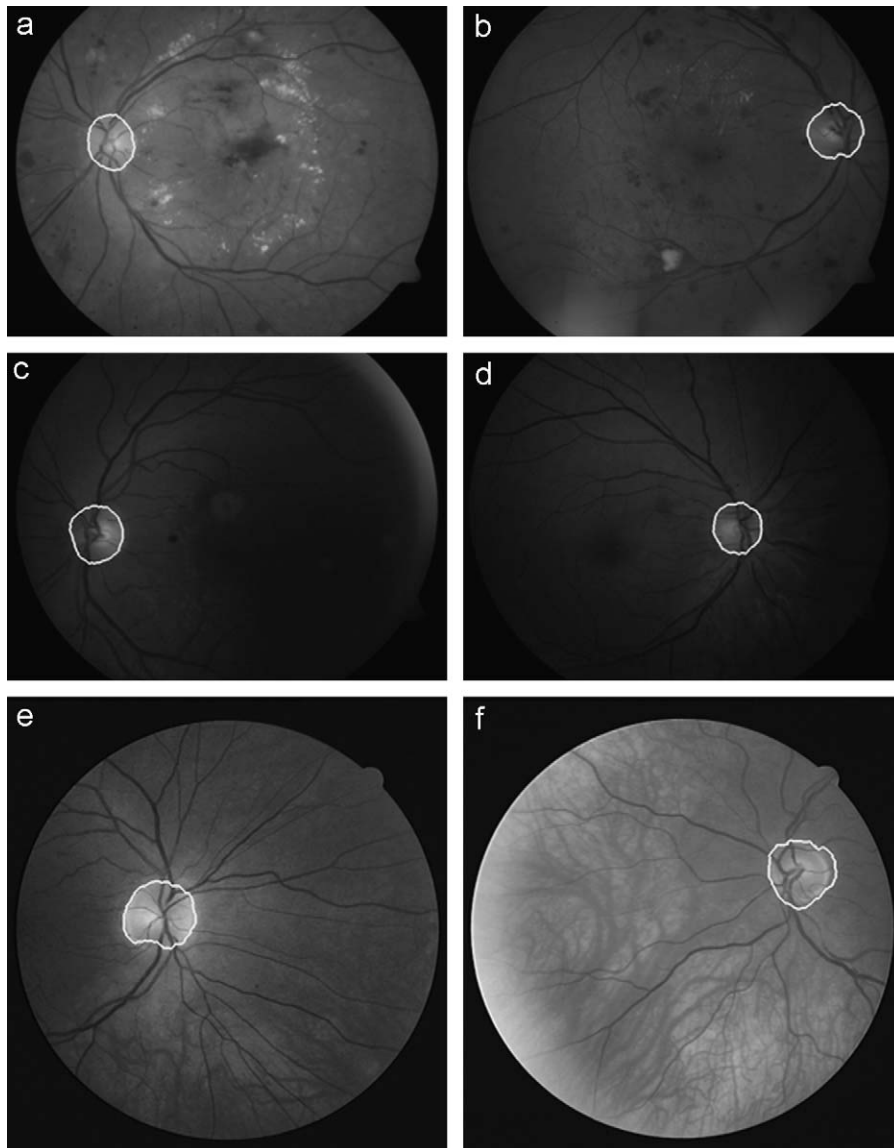


Fig. 11. The detection of the optic disk boundaries in various situations. (a), (b) Detected optic disk boundary on an image containing diabetic lesions. (b), (c), (f) Detected optic disk boundary on images containing varying illumination conditions. (d), (e), (f) Detected optic disk boundary on images taken under varying acquisition conditions (i.e. on optic disk centered images).

obtained correct optic disk location in 100% of the images, 41.47% of mean optic disk overlap. For the DIARETDB1 database, the optic disk was correctly located in 97.75% of the images with a mean overlap of 43.65%. These results indicate that an improvement has been obtained over other methods proposed by literature. Specially because our method tries not only to detect the optic disk, but also to detect the optic disk contour (i.e. boundaries), without having to assume any pre-defined shape (e.g. a circle of a predefined size). In order to evaluate our results quantitatively, the optic disk segmentation results were compared to other approaches using quantitative measures such as mean absolute distance (MAD) and area overlap, confirming the benefits offered by our approach. Furthermore, our method has been designed to detect optic disk features even when diabetic lesions or illumination artifacts are present in the retina image. However, it was verified experimentally that large opaque lesions (e.g. large hemorrhages) tend to reduce the vascular tree visibility, and may impact negatively on our method results.

The experimental results are promising, and the proposed method appears to be robust to the different imaging conditions existing in both image databases tested, since the same parameter values were used in all experiments. Besides, the method does not require a vessels elimination stage in order to reduce the vessels influence in the optic disk location or in the detection of its rim. Usually, the optic disk location requires some parameter fine tuning in most methods available in the literature, but this additional parameter adjustment is not necessary in our method. On the other hand, our proposed approach requires the computation of specific preprocessing stages (e.g. enhancement and smoothing steps to detect the vascular tree).

Future work will concentrate on the detection of other important retina structures, like the fovea, based on the optic disk boundary detection obtained with the method proposed in this paper.

Conflict of interest statement

None declared.

Acknowledgments

The authors wish to thank all the anonymous referees for their valuable comments that have helped us to improve this paper, and to the DRIVE and DIARETDB1 project teams for making available their image databases on the Internet. Many thanks to Carmen Alina Lupaşcu et al. for providing their resulting images. Also, the authors are particularly grateful to CNPq (Conselho Nacional de Desenvolvimento Científico e Tecnológico, Brazil) for financial support.

References

- [1] N. Patton, T.M. Aslam, T. MacGillivray, I.J. Deary, B. Dhillon, R.H. Eikelboom, K. Yegesan, I.J. Constable, Retinal image analysis: concepts, applications and potential, *Progress in Retinal and Eye Research* 25 (1) (2006) 99–127.
- [2] T.Y. Wong, R. Klein, A.R. Sharrett, B.B. Duncan, D.J. Couper, B.E. Klein, L.D. Hubbard, J. Nieto, Retinal arteriolar diameter and risk for hypertension, *Annals of Internal Medicine* 140 (4) (2004) 248–255.
- [3] A. Ruggeri, E. Grisan, M.D. Luca, An automatic system for the estimation of generalized arteriolar narrowing in retinal images, in: 29th Annual International Conference of the IEEE EMBS, IEEE, Cité Internationale, Lyon, France, 2007, pp. 6463–6466.
- [4] K.A. Rezai, S.C. Patel, D. Elliott, M.A. Becker, Rheumatoid hyperviscosity syndrome: reversibility of microvascular abnormalities after treatment, *American Journal of Ophthalmology* 134 (2002) 130–132.
- [5] A. Bade, J.J. Pizzimenti, Interdisciplinary management of diabetic eye disease: a global approach to care, *The Internet Journal of Allied Health Sciences and Practice* 5 (1) (2007) 1–11.
- [6] D. Vallabha, R. Dorairaj, K. Namuduri, H. Thompson, Automated detection and classification of vascular abnormalities in diabetic retinopathy, *Signals, Systems and Computers* 2 (2004) 1625–1629.
- [7] T.A. Ciulla, A.G. Amador, B. Zinman, Diabetic retinopathy and diabetic macular edema, *Diabetes Care* 26 (9) (2003) 2653–2664.
- [8] T. Kauppi, V. Kalesnykiene, J.-K. Kämäräinen, L. Lensu, I. Sorri, A. Raninen, R. Voutilainen, H. Uusitalo, H. Kälviäinen, J. Pietilä, DIARETDB1 diabetic retinopathy database and evaluation protocol, in: *Medical Image Understanding and Analysis (MIUA)*, 2007, pp. 61–65.
- [9] F. Laliberté, L. Gagnon, Y. Sheng, Registration and fusion of retinal images—an evaluation study, *IEEE Transactions on Medical Imaging* 22 (5) (2003) 661–673.
- [10] V.E. Markaki, P.A. Asvestas, G.K. Matsopoulos, N.K. Uzunoglu, Application of the Kohonen network for automatic point correspondence in retinal images, in: 29th Annual International Conference of the IEEE EMBS, IEEE, Cité Internationale, Lyon, France, 2007, pp. 6467–6470.
- [11] H. Li, O. Chutatape, Automated feature extraction in color retinal images by a model based approach, *IEEE Transactions on Biomedical Engineering* 51 (2) (2004) 246–254.
- [12] E.M. Hoffmann, L.M. Zangwill, J.G. Crowston, R.N. Weinreb, Optic disk size and glaucoma, *Survey of Ophthalmology* 52 (1) (2007) 32–49.
- [13] K.W. Tobin, E. Chaum, V.P. Govindasamy, T.P. Karnowski, Detection of anatomic structures in human retinal imagery, *IEEE Transactions on Medical Imaging* 26 (12) (2007) 1729–1739.
- [14] M. Foracchia, E. Grisan, A. Ruggeri, Detection of optic disc in retinal images by means of a geometrical model of vessel structure, *IEEE Transactions on Medical Imaging* 23 (10) (2004) 1189–1195.
- [15] M. Park, J.S. Jin, S. Luo, Locating the optic disc in retinal images, in: *Proceedings of the International Conference on Computer Graphics, Imaging and Visualisation*, IEEE, Sydney, Australia, 2006, pp. 14–145.
- [16] C. Sinthanayothin, J.F. Boyce, H.L. Cook, T.H. Williamson, Automated localisation of the optic disc, fovea, and retinal blood vessels from digital colour fundus images, *British Journal of Ophthalmology* 83 (1999) 902–910.
- [17] T. Walter, J.-C. Klein, P. Massin, A. Erginay, A contribution of image processing to the diagnosis of diabetic retinopathy—detection of exudates in color fundus images of the human retina, *Transactions on Medical Imaging* 21 (10) (2002) 1236–1243.
- [18] A.A.-H.A.-R. Yousif, A.Z. Ghalwash, A.A.S.A.-R. Ghoneim, Optic disc detection from normalized digital fundus images by means of a vessels' direction matched filter, *IEEE Transactions on Medical Imaging* 27 (1) (2008) 11–18.
- [19] J. Lowell, A. Hunter, D. Steel, A. Basu, R. Ryder, E. Fletcher, L. Kennedy, Optic nerve head segmentation, *IEEE Transactions on Medical Imaging* 23 (2) (2004) 256–264.
- [20] M. Niemeijer, M.D. Abràmoff, B.V. Ginneken, Segmentation of the optic disc, macula and vascular arch in fundus photographs, *IEEE Transactions on Medical Imaging* 26 (2007) 116–127.
- [21] A. Sopharak, B. Uyyanonvara, S. Barmanb, T.H. Williamson, Automatic detection of diabetic retinopathy exudates from non-dilated retinal images using mathematical morphology methods, *Computerized Medical Imaging and Graphics* 32 (2008) 720–727.
- [22] A.D. Fleming, K.A. Goatman, S. Philip, J.A. Olson, P.F. Sharp, Automatic detection of retinal anatomy to assist diabetic retinopathy screening, *Physics in Medicine and Biology* 52 (2) (2007) 331–345.
- [23] E.J. Carmona, M. Rincón, J. García-Feijoó, J.M.M. de-la Casa, Identification of the optic nerve head with genetic algorithms, *Artificial Intelligence in Medicine* 43 (3) (2008) 243–259.
- [24] C.A. Lupaşcu, D. Tegolo, L.D. Rosa, Automated detection of optic disc location in retinal images, in: 21st IEEE International Symposium on Computer-Based Medical Systems, IEEE, University of Jyväskylä, Finland, 2008, pp. 17–22.
- [25] DRIVE: Digital Retinal Images for Vessel Extraction. URL: <<http://www.isi.uu.nl/Research/Databases/DRIVE/>>.
- [26] B. Jähne, H. Haußecker, P. Geißler, *Handbook of Computer Vision and Applications: Signal Processing and Pattern Recognition*, vol. 2, Academic Press, New York, 1999.
- [27] M. Wirth, M. Fracchini, J. Lyon, Contrast enhancement of microcalcifications in mammograms using morphological enhancement and non-flat structuring elements, in: 17th IEEE Symposium on Computer-Based Medical Systems, IEEE Computer Society, Silver Spring, MD, 2004.
- [28] H. Jlassi, K. Hamrouni, N. Ellouze, Blood vessels segmentation in retina image using mathematical morphology and the STFT analysis, in: *International Conference on Information and Communication Technologies: From Theory to Applications*, second ed., vol. 1, IEEE, New York, 2006, pp. 1130–1134.
- [29] T. Walter, J.-C. Klein, Segmentation of color fundus images of the human retina: detection of the optic disc and the vascular tree using morphological techniques, *Medical Data Analysis*, vol. 2199/2001, Springer, Berlin, Heidelberg, 2001, pp. 282–287.
- [30] E.R. Dougherty, R.A. Lotufo, *Hands-on Morphological Image Processing*, vol. TT59, SPIE Publications, 2003.
- [31] M. Sonka, J.M. Fitzpatrick, *Handbook of Medical Imaging: Medical Image Processing and Analysis*, vol. 2, SPIE Press, 2000.
- [32] K. Stapor, A. Świtonski, R. Chrastek, G. Michelson, Segmentation of fundus eye images using methods of mathematical morphology for glaucoma diagnosis, in: ICSC 2004, 4th International Conference, Kraków, Poland, June 6–9, 2004, *Proceedings, Part IV, Lecture Notes in Computer Science*, vol. 3039/2004, Springer, Berlin, Heidelberg, 2004, pp. 41–48.

- [33] J.M. Seo, K.K. Kim, J.H. Kim, K.S. Park, H. Chung, Measurement of ocular torsion using digital fundus image, in: Proceedings of the 26th Annual International Conference of the IEEE EMBS, San Francisco, USA, 2004, pp. 1711–1713.
- [34] G.B. Kande, P. Subbaiah, T. Savithri, Segmentation of exudates and optic disc in retinal images, in: Sixth Indian Conference on Computer Vision, Graphics and Image Processing, 2008, ICVGIP, IEEE Computer Society, Bhubaneswar, India, 2008, pp. 535–542.
- [35] V. Chalana, D.T. Linker, D.R. Haynor, Y. Kim, A multiple active contour model for cardiac boundary detection on echocardiographic sequences, *IEEE Transactions on Medical Imaging* 15 (3) (1996) 290–294.